ELSEVIER

International Journal of Heat and Fluid Flow 20 (1999) 255–267

International Journal of HEAT AND FLUID FLOW

www.elsevier.com/locate/ijhff

# Vortex structure and heat transfer in turbulent flow over a wall-mounted matrix of cubes

E.R. Meinders *[,1], K. Hanjalić

*Faculty of Applied Physics, Delft University of Technology, P.O. Box 5046, 2600 GA Delft, The Netherlands*

**Abstract**

The paper reports on the turbulent flow structure and the distribution of the local surface heat transfer coefficient of a cube placed in a spatially periodic in-line matrix of cubes mounted on one of the walls of a plane channel. Infrared thermography was applied to measure the surface temperature at the cube walls, from which the distribution of the local heat transfer coefficient was determined. The velocity field and its structure were evaluated from Laser Doppler Anemometry (LDA) measurements and flow visualizations. The spatial periodicity was confirmed from flow field and heat transfer measurements across the entire matrix. The results showed that the flow has a marked vortex structure only in the immediate proximity of the cube, while the flow above the cube and in the streamwise corridors was only mildly distorted, except for a high level of turbulence intensity. Flow separation at the sharp leading top and side edges led to flow recirculations with subsequent flow reattachment at these faces. Reattachment of the top shear layer at the channel floor downstream of the cube produced a two-cell structure in the inter-obstacle space: an arc-type vortex in the wake of the upstream cube and a horseshoe-type vortex in front of the downstream cube. Flow instabilities caused vortex shedding at the side faces of the cube which led to periodic motions in its wake. The measured Strouhal number showed a constant value of $St = 0.109$ over the range of Reynolds numbers considered. The observed local flow structure, in particular flow separation and reattachment, caused marked variation in the distribution of the local heat transfer coefficient, with large gradients detected particularly at the top and side faces of the cube. 

## Notation

| | |
|---|---|
| $D$ | channel height (m) |
| $f$ | frequency (Hz) |
| $h$ | heat transfer coefficient (W/m$^2$K) |
| $\overline{h}$ | average $h$ (W/m$^2$K) |
| $H$ | cube size (mm) |
| $k$, $k_{2D}$ | turbulent kinetic energy (m$^2$/s$^2$) |
| $Re_H$ | Reynolds number ($=u_B H/\nu$) |
| St | Strouhal number ($=fH/u_B$) |
| $u_B$ | bulk velocity (m/s) |
| $\overline{u}$, $\overline{v}$, $\overline{w}$ | mean velocity (m/s) |
| $\overline{u'^2}$, $\overline{v'^2}$, $\overline{w'^2}$ | Reynolds normal stress (m$^2$/s$^2$) |
| $\overline{u'v'}$, $\overline{u'w'}$ | Reynolds shear stress (m$^2$/s$^2$) |
| $x$ | coordinate in streamwise direction (m) |
| $y$ | coordinate in spanwise direction (m) |
| $z$ | coordinate in normal direction (m) |
| *Greek* | |
| $\nu$ | kinematic viscosity (m/s$^2$) |
| $\Phi$ | power spectral density |

## 1. Introduction

Turbulent flow over and convective heat transfer from a wall-mounted matrix of cubes have been widely adopted as an idealised representation of various practical situations encountered in engineering. A typical example is electronics cooling, where the cube matrix has been adopted as a model for densely packed printed circuit boards. The matrix flow involves complex vortical structures and several generic flow phenomena, such as impingement, separation, recirculation and reattachment, where the surface heat transfer from the cubes displays notable dissimilarity from the momentum transport. The involved spatially periodic flow boundary conditions make this configuration well suited for benchmarking purposes to validate turbulence models and numerical methods.

Flows over isolated, wall-mounted cubes have been subject to several past investigations. Castro and Robins (1977) measured the flow velocity around a single cube mounted on a flat plate with different oncoming boundary layers. It was shown that the extent of the wake recirculation and the size of the vortex on top of the obstacle were strongly dependent on the boundary layer thickness of the oncoming flow. The flow around a single wall-mounted cube in a fully developed turbulent channel flow was investigated experimentally by Hussein and Martinuzzi (1996), Larousse et al. (1991), Martinuzzi (1992) and Martinuzzi and Tropea (1993). The Reynolds number was $Re_H = 40.000$, based on the cube height ($H = 2.5$

* Corresponding author. E-mail: meinders@natlab.research.philips.com.

[1] Present address: Philips Research, Material and Process Technology, Prof. Holstlaan 4, Building WB 151, 5656 AA Eindhoven, The Netherlands.

0142-727X/99/$ – see front matter 
PII: S0142-727X(99)00016-8

cm) and the bulk velocity. The channel height-to-cube ratio was 2. The major flow features were well documented: the horseshoe vortex induced at the windward face, the arc-shaped vortex in the wake of the cube and the flow recirculations at the top and side faces of the cube. Further, the studies included a detailed description of the Reynolds stresses and higher order moments. It was found that the horseshoe vortex region was unstable but non-periodic which caused bimodal velocity distributions. Vortex shedding was detected in the wake of the cubical obstacle.

The flow structure around multiple-obstacle configurations in a channel flow received little attention in the literature. Okamoto et al. (1996) studied the flow field in a matrix of surface-mounted square blocks of width $D = 23$ mm and height $H = 5$ mm placed in a boundary layer. The face-to-face distance $S$ (in both the streamwise and the spanwise direction) was varied as $S/H = 2$, 3, 5, 7, 10 and 13 to investigate the different flow regimes as imposed by the different distances between the blocks. The Reynolds number was constant for all configurations studied, $\mathrm{Re}_H = U_\infty H/\nu = 990$, where $U_\infty$ denotes the freestream velocity. They used a two-colour Laser Doppler Anemometer (LDA) to measure the time-mean velocities and turbulence intensities around the protruding obstacles. The study showed that for $S/H < 5$ the flow did not reattach at the channel floor and that the inter-obstacle space was fully covered by a large flow recirculation. Reattachment at the channel floor of the separated shear layer was detected at $S/H > 7$. They found that the configuration of blocks with spacing $S/H = 7$ had maximum turbulence intensities around the blocks.

In an earlier paper (Meinders et al., submitted) we reported on the convective heat transfer characteristics of a single wall-mounted cube in a developing turbulent channel flow for a Reynolds number range of $2750 < \mathrm{Re}_H < 4970$, based on the cube size $H = 15$ mm and the bulk velocity. It was shown that the distributions of the local heat transfer coefficient exhibit large gradients, in particular at the top and side faces of the cube. This strong variation was caused by the specific flow structure around the cube. For example, flow separation and reattachment at the top and side faces of the cube caused significant differences in the local heat transfer. Besides this large variation at the individual faces, substantial differences were shown to exist between the face-averaged heat transfer coefficients for the different faces of the cube.

Several studies in the literature reported on the average convective heat transfer from isothermal three-dimensional protrusions in a matrix arrangement. Anderson and Moffat (1990, 1992) and Moffat and Anderson (1990) dealt with a matrix of aluminium cubes and flat packs mounted on an insulating channel wall. The concept of the adiabatic heat transfer coefficient was successfully applied aimed at eliminating the influence of the upstream thermal boundary conditions. Different parameters were varied: the channel height with respect to the obstacle height, the obstacle sizes (cubes and flat packs), the spanwise and streamwise separation between the components and the Reynolds number. One of the differences, as compared to the present study, is the lack of spatial periodicity; they examined a matrix with a limited number of protrusions. Nevertheless, these studies provided much insight into the convective heat transfer for this kind of multiple element configuration. It was shown that a fully developed heat transfer regime was obtained after four or five rows of cubes. Garimella and Eibeck (1990a, b) and Morris and Garimella (1997) also focussed on the average convective heat transfer from isothermal rectangular prismatic copper cuboids on a flat plate in a water channel. Their studies included variation of different geometrical parameters (e.g. the channel height, streamwise and spanwise distance between the obstacles, in-line and staggered arrangements) and the flow Reynolds number. The range of Reynolds numbers considered covered laminar, transitional and turbulent channel flows. They observed that the convective heat transfer is significantly dependent on the streamwise separation, channel height and Reynolds number.

Most previous studies of multiple three-dimensional protrusions in a matrix arrangement focused primarily on the cube-average convective heat transfer from isothermal protrusions. Further, the papers cited concentrated mainly on isolated wall-mounted cubes in a channel flow. In contrast, this paper deals with the flow structure around and the local convective heat transfer from a cube located in a spatially periodic in-line matrix of cubes. In addition to providing details of the velocity and Reynolds stress fields and distributions of the local heat transfer coefficient, we analysed the similarity (or a lack of it) between the momentum transfer in the near-wall flow region and the local surface heat transfer.

## 2. Experimental setup

The experiments were performed in a wind tunnel with a rectangular test section with the height of 600 mm and width of 51 mm. A matrix of cubes with size 15 mm, spaced equidistantly at 45 mm (face-to-face) in both the streamwise and spanwise direction ($S_x/H = S_z/H = 4$), was mounted on one of the vertical channel walls. A schematic sketch of the configuration (rotated into a horizontal plane) is given in Fig. 1. The matrix consisted of a total of $25 \times 10$ cubes in the streamwise and the spanwise direction, respectively. The oncoming flow was conditioned with a set of honeycombs and meshes. The inflow conditions were controlled by tripping the boundary layer approximately 1 m upstream of the first row of cubes.

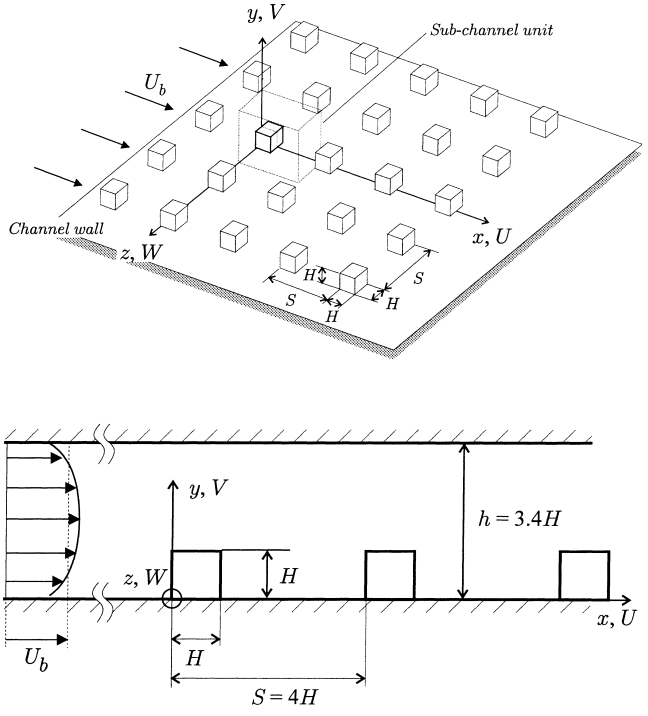


Fig. 1. Three-dimensional sketch of the matrix configuration of cubes on the channel wall (upper plot) and the side view of the configuration (lower plot).

The flow and heat transfer measurements were performed around the 18th row counted from the inlet, at mid-position of the channel. This location ensured a fully developed flow in both the streamwise and the spanwise direction independent of the inflow conditions, as was confirmed with velocity measurements at several locations across the entire matrix. The origin of the local coordinate system is defined in Fig. 1. The $x$, $y$ and $z$ directions are in the streamwise, normal and spanwise direction, respectively. The mounting base was machined from formaldehyde which had a low thermal conductivity of 0.33 W/mK. This low value minimised the conductive heat losses through the base plate. The flow field was measured with an LDA at a Reynolds number of $Re_H = 3854$, based on the cube height and the bulk velocity. Smoke and oil-film visualizations, as well as the measurements of the frequency of shedding vortices, were performed in a broader range of Reynolds numbers (1000–7000) to complement the LDA flow field measurements.

The mean velocity and Reynolds stress components were measured with a two-component back-scatter LDA (TSI 9230/9201) mounted on a three-axis traversing system. The experimental rig was not suitable for using a forward-scatter LDA system. It is believed that the backscatter LDA system with the optical focal length of 120.5 mm enabled a good signal-to-noise ratio. The beam inter-section angle was relatively large, i.e. $0.380 \pm 0.001$ rad, determined from theodolite measurements and laser beam mapping (Meinders, 1998c). The involved measuring volume had dimensions of 0.20 mm length and 0.04 mm diameter. This small measuring volume minimised velocity gradient bias (less than 2%). In case of larger measuring volumes, this bias can be significant due to relatively large velocity gradients encountered in the vicinity of the cubes.

The measurement of the flow reversal was enabled by selecting a preshift frequency of 5 MHz. A mixture of atomised glycerol/water seeded the flow (the particle sizes were between 0.1 and 1 μm). A TSI IFA-750 was used for data acquisition. Typical data rates ranged between 400 and 800 Hz. Arithmetic averaging of the Poisson-distributed realizations for obtaining the time-averaged quantities introduces velocity bias. Two different weighting methods were assessed, an inter-arrival time weighting and inverse velocity weighting, to obtain more appropriate estimates of the time-averaged quantities. The inter-arrival time weighting only gives reliable results for relatively large data rates (Absil, 1996). Although data rates in this study were fairly large (the aforementioned range of 400–800 Hz) the inverse velocity weighting was preferred since it provides results without severe constraints (Meinders, 1998c).

The regular laser probe orientation, perpendicular to the channel floor, allowed the direct measurement of the streamwise $u$ and the spanwise $w$ velocity components. The normal velocity component $v$ was measured with a specially designed prism-cube. It consisted of two prisms, one made of crystal glass and the other of a copper alloy, with a mirror at the diagonal plane (hypothenuse). A simplified schematic sketch of this prism cube is given in Fig. 2 (the refraction of the laser beams is omitted to simplify the drawing). The mirror at the hypothenuse plane reflects the laser beams at an angle of exactly 90° and creates a measuring volume in the inter-obstacle spacing (in front of the prism cube). For the orientation shown in Fig. 2, a traverse movement of the laser probe in the normal direction results in a translation of the measuring volume in the streamwise ($x$) direction. Vertical and horizontal movements of the laser probe equally cause a translation of the measuring volume in the vertical and normal direction, respectively. The reflected measuring volume enables the measurement of the spanwise $w$ and normal $v$ velocity components in the coincidence mode. A 90° rotation of the prism cube

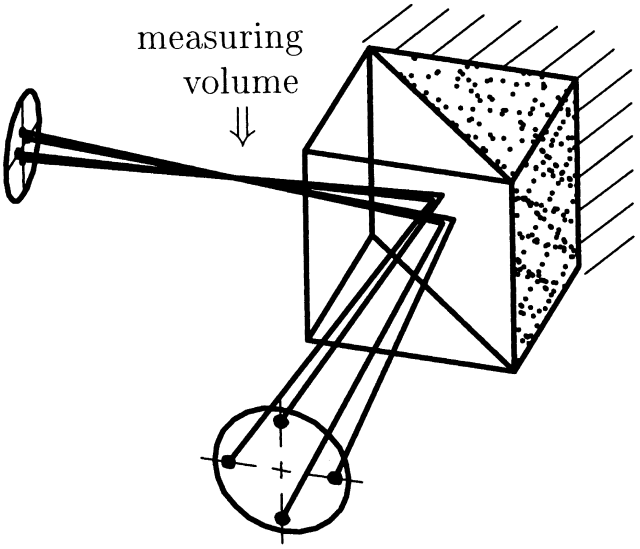


Fig. 2. Schematic diagram of the prism cube used for the measurement of the normal velocity component ($v$).

enables the measurement of the streamwise $u$ and normal $v$ velocity components in the region adjacent to the sides of the cube. Measurement of $w$ and $v$ in the wake region was possible with another 90° of rotation. The technique is geometrically constrained by the size of the cube and the inter-section angle. Measurements are only possible in a triangular region, bound by the side faces of the cube. Small discrepancies of the 45° angle cause different refractions of the individual laser beams which consequently cause a shift of the waist (the minimum cross-section of the laser beam). The resulting misalignment of the measuring volume may cause fringe gradients which subsequently lead to artificial turbulence intensities (Absil, 1996). However, the machine specifications were better than 0.01° which excluded this error. The position error of the measuring volume caused by small deviations of the 90° reflections is estimated to be within 1%. In order to obtain a quantifiable validation of this estimation, some velocity and Reynolds stresses data measured with the prism cube were duplicated with the LDA system in the standard orientation. These results confirmed that the accuracy of the prism-cube results is similar to that of the regular LDA-results. In addition to this method, normal velocities were obtained from a reconstruction technique which is primarily based on different LDA measurements with an inclined optical probe at different inclination angles. These inclined measurements required a special arrangement of the optics to ensure accurate results. From uncertainty analysis, it was derived that the reconstructed mean normal velocities were less accurate than the prism-cube results, i.e. roughly 10%. A detailed description of both the techniques is given in Meinders (1998c).

Coincidence windows between 50 and 100 μs were used to resolve the Reynolds shear stresses $\overline{u'v'}$, $\overline{u'w'}$ and $\overline{v'w'}$. The first and higher order statistical quantities were determined from 10,000 samples which gave a statistical uncertainty of less than 0.02 m/s. The maximum experimental uncertainty is estimated to be at maximum 5% for the mean velocities and 10% for the Reynolds normal and shear stresses based on methods reviewed in the literature (Absil, 1996; Durst et al., 1976).

Oil-film visualizations were performed to complement the LDA measurements. A visualization mixture was made from jet fuel, toner and low-viscosity transmission oil. During the course of the experiment, the mixture accumulates at locations on the surface where the shear stress is low (for example

around flow separation and reattachment), and is removed at locations subjected to high shear stress. Evaporation of the jet fuel (after several minutes) causes a significant viscosity increase of the mixture which causes a fixation of the visualization pigment (and thus the streakline pattern) to the wall surface. This enables the identification of critical points and lines in the surface plot.

Heat transfer was measured using specially made heat transfer assemblies which consisted of cubes made from an internally heated copper cubical core covered by a layer of epoxy of thickness 1.5 mm. The local convective heat fluxes through the outer surface of the cube were determined from a three-dimensional analysis of the temperature distribution in the epoxy layer with temperature boundary conditions for both the internal and external surface. The internal surface was kept at a constant temperature because of the high thermal conductivity of the copper core. The external boundary conditions were measured with infrared thermography. The experimental method and the measurement techniques were discussed in previous works (Meinders et al., 1997, 1998a; Meinders, 1998c). The technique involved an experimental uncertainty of 5–10% in the heat transfer coefficients.

## 3. Flow characteristics

A consistency validation was performed from mass conservation at four different sub-planes at periodic up- and downstream locations. These planes ($x/H = -1.5$ and 2.5, $z/H \geqslant 0$ and $x/H = -1.5$ and 2.5, $z/H \leqslant 0$) are centred around the local symmetry plane $z/H = 0$ at the middle of the cube in question. The spatially periodic and symmetric situation requires a necessarily equal mass flow rate through the four sub-planes. For each sub-section, seven velocity profiles in normal direction were measured at equidistant locations. The profiles were determined at the following locations in the four sections: $x/H = -1.5$ and 2.5, $z/H = 0, \pm 0.33, \pm 0.66, \pm 1, \pm 1.33, \pm 1.66$ and $\pm 2$. The distance between the individual stations (5 mm) was sufficiently small to ensure a reasonably accurate estimate of the velocity gradients in the spanwise direction. The integrations of the velocity profiles yielded an average mass flow rate of $6.85 \times 10^{-3}$ kg/s with deviations of less than 1%, providing a proof of a good spatial periodicity and symmetry. The average velocity, derived from the ratio of the mass flow rate and the integration area, yielded a value of $u_B = 3.86$ m/s. The Reynolds number based on the bulk velocity and the cube size was $Re_H = 3854$. The spatial periodicity was further confirmed with LDA measurements across the entire matrix of cubes in both the spanwise and streamwise direction. The observed deviations were also within 1%. Duplications of the velocity and Reynolds stress data for several stations demonstrated the reproducibility of the measurements (the discrepancies between the measurements were less than 1%).

### 3.1. General flow structure

An impression of the flow field around the cube was derived from the LDA measurements and flow visualizations, Fig. 3. Distinct vortex structures were only observed in the immediate proximity of the obstacle, while the core flow in the region above the cubes and in the streamwise corridors between them remained almost undistorted. The flow in the inter-obstacle space is characterized by a two-cell structure arising from the reattachment at the channel floor of the shear layer separated at the leading top edge of the upstream cube. The long-term averaged flow reattachment occurred at a distance of approximately 1.5 cube heights ($x/H = 2.5$) from the leeward face. This shear layer bounds the vortex in the wake of the upstream cube. A horseshoe type of vortex was formed at the windward face of the cube and was deflected downstream along both sides of the cube, weakening further downstream through the interaction with the counter-rotating vortices along the neighbouring cubes.

A vector plot of the velocity field in the symmetry plane $z/H = 0$ is given in Fig. 4. The plot is a collection of results obtained from two different measurement techniques. The vectors, located in the two triangular areas upstream and downstream of the cube, are composed of the normal velocities measured with the prism cube and the streamwise velocities obtained from the direct measurement with the laser probe in the standard orientation. The figure shows that due to the geometrical constraints imposed by the prism cube, the normal velocities could only be measured in the limited triangular regions. The other vectors were obtained with the reconstruction technique from two separate velocity measurements acquired at different inclination angles of the laser probe. Although the results obtained with the reconstruction technique were less accurate than those acquired with the prism cube, the agreement between the results in the overlapping region provides sufficient evidence of the reliability of the reconstruction method. The vortex structures can be readily identified from the vector plot in Fig. 4. A downwash of the flow, originating from the horseshoe vortex, is indicated by negative velocities in the proximity of the windward cube wall. The wake flow is dominated by the arc-shaped vortex, causing a strong upwash close to the leeward face. The velocity vectors close to the top

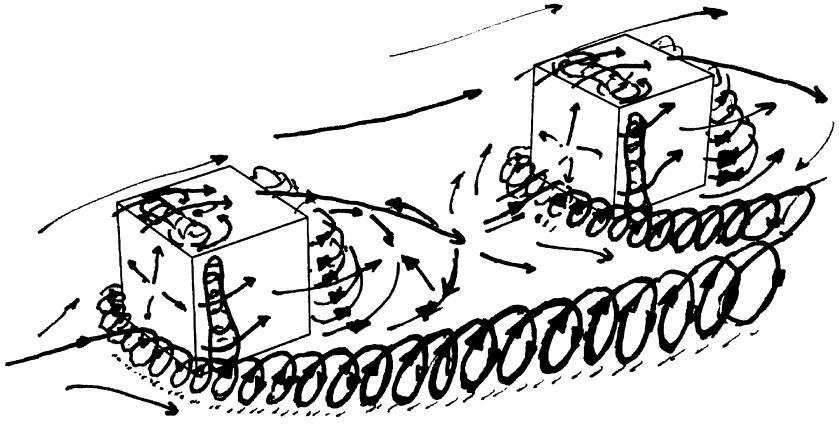

Fig. 3. Artists' impression of the three-dimensional flow pattern around the cube for one spatial period in the matrix.

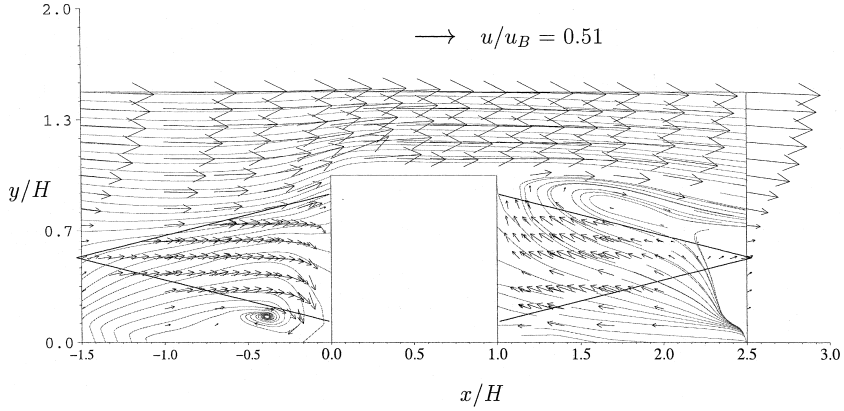


Fig. 4. Long-term averaged vector plot with streamlines in the $xy$-plane for one spatial period in the matrix at $z/H = 0$. The vectors in the triangular region were obtained from measurements with the prism cube, the other vectors were determined with the reconstruction method from inclined velocity measurements.

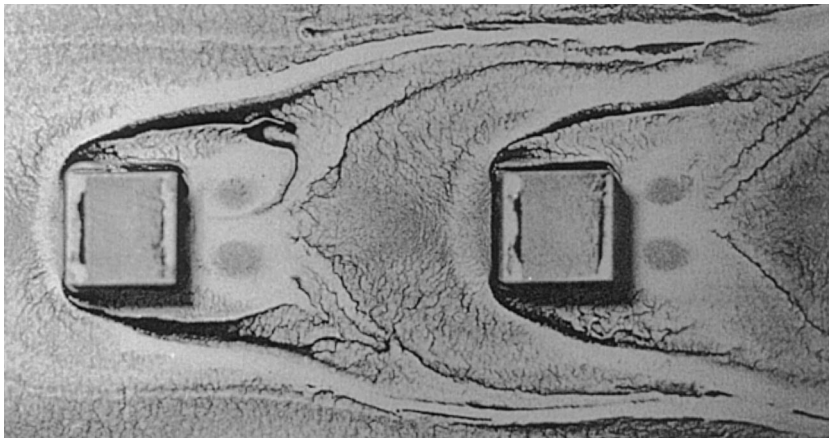

Fig. 5. Oil-film visualization of the surface streaklines in the matrix flow.

leading edge, Fig. 4, indicate that the flow separated and created a recirculation bubble in the vicinity of the leading top edge. Although it was not possible to measure this with the LDA set-up, the flow reversal was apparent from the surface streak lines of the oil-film visualizations given in Fig. 5. The top face shows a pigment removal close to the leading edge which originates from the recirculation flow. Flow reattachment is found at approximately 4 mm downstream of the leading edge, as appears from the more or less smeared pigment pattern.

A further analysis of the visualization in Fig. 5 reveals the imprint of the horseshoe-type vortex in front of the obstacle as the white line, bending around the cube along the separation line. This vortex joins the horseshoe vortex generated upstream in the corridor region, see Fig. 5. The influence of the extensions of other horseshoe vortices, induced in front of the cubes more upstream, has diminished. At $x/H = 0.5$, both co-rotating horseshoe vortices interact with each other, but do not fully merge. If they are of comparable strength, the interaction at this location leads to negative normal velocities close to the obstacle side face, positive values at the symmetry line $z/H = 2$ and zero values at the interface. This hypothesis is supported by the $v$-measurements given in Fig. 6 in the $yz$-plane at $x/H = 0.5$. Note that the traverses shown were measured with the prism cube. For this orientation, the measurement was also geometrically constrained. Negative velocities were found around $z/H = 0.5$ to 1.0 due to the downwash of the first horseshoe vortex; the velocity decays gradually with an increase in height $y/H$. At $z/H = 1.4$, the horseshoe vortex interacts with the extensions of the downstream horseshoe vortex: the upwash of the inner vortex more or less nullifies the downwash of the outer horseshoe vortex. Because of the flow symmetry, the effects of the two extensions of the upstream horseshoe vortices are superimposed at $z/H = 2$, resulting in an acceleration of the flow in the normal direction.

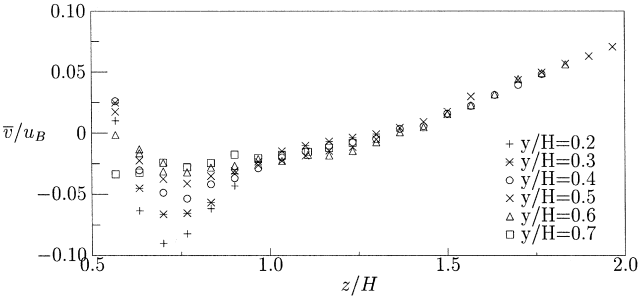


Fig. 6. Profiles of the normal velocity $\overline{v}$ at $x/H = 0.5$ at different heights $y/H$.

Vector plots of the streamwise and spanwise velocities $u$ and $w$ with superimposed trajectories are given in Fig. 7 for one half of a spatial period in the matrix for $y/H = 0.25$, 0.50 and 0.75. The flow symmetry was verified with velocity measurements across the entire $xz$-plane at different stations showing negligible differences. This symmetry allowed us to concentrate on only one symmetric half of the spatially periodic domain. An almost undistorted corridor region between the cube arrays is visible in the plots. The oncoming flow is bent towards the cube sides to separate at the leading side face, creating a small recirculation bubble close to the leading side edge. As a consequence, the separated shear layer reattaches at approximately 5 mm downstream from the side edge. This was demonstrated by the measurements of the streamwise component at 0.5 mm distance from the wall ($z/H = 1.07$). These measurements showed a negative velocity up to 5 mm distance ($x/H = 1/3$) from the leading edge, Fig. 8. The vortex tubes are aligned along the leading side edges with their origins at the channel floor. Their imprints can be seen from the oil-film picture as the nodal pigment accumulates close to the leading side edges (see Fig. 5). The oil-film pattern at the side faces (not shown in the paper) showed a white feather-type imprint of the side recirculation close to the leading edge. This structure is qualitatively similar to that found for a single cube in a developing turbulent channel flow (Meinders, 1998c).

The wake flow shows the recirculation of the arc-type vortex. The results at the three different levels $y/H$ show a gradual growth of the recirculation area towards the channel wall. An extrapolation of the line where the streamwise velocity changes sign, gives a reattachment point at $x/H = 2.5$.

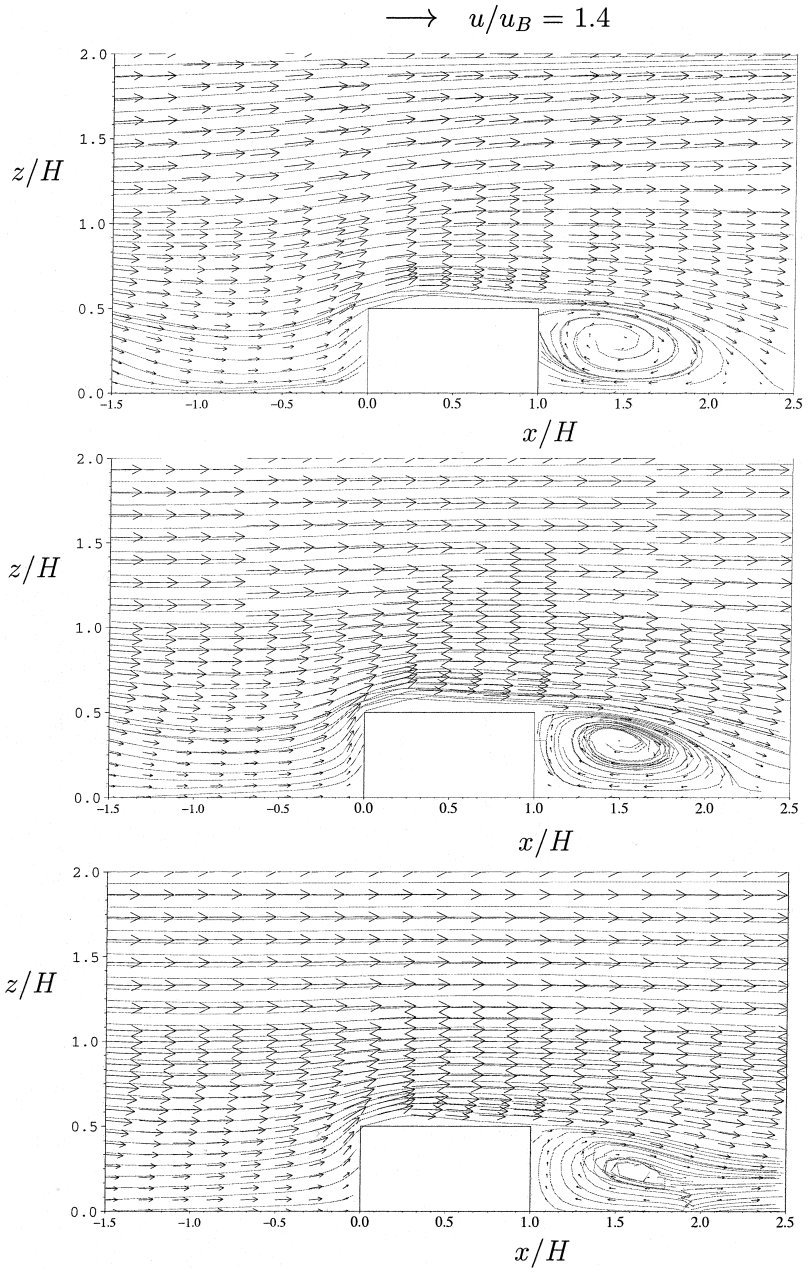


Fig. 7. Vector plots with streamlines in the $xz$-plane for one half of a spatial period in the matrix for $y/H = 0.25$ (first), $y/H = 0.50$ (second) and $y/H = 0.75$ (third).

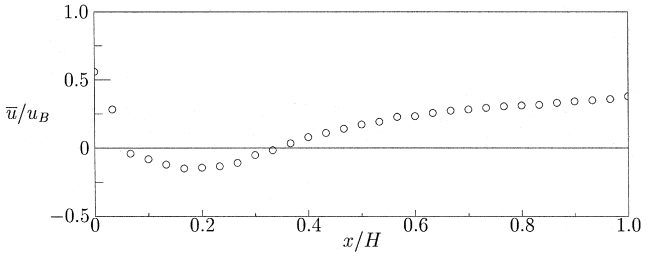


Fig. 8. Profile of the mean velocity $\overline{u}$ at $y/H = 0.5$ and $z/H = 1.07$.

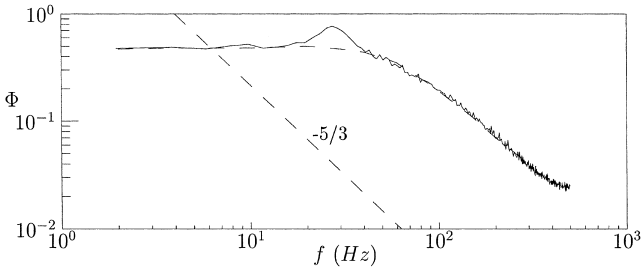


Fig. 9. Power density spectrum of the $w$-component at the station $x/H = 2$, $y/H = 0.5$, $z/H = 0.5$ for $u_B = 3.9$ ms.

The oil-film visualization in the wake of the cube indicates two pigment concentrations which refer to two counter-rotating foci. These vorticity concentrations are the imprints of the wake vortex and its location agrees reasonably well with the LDA measurements at $y/H = 0.25$, extrapolated towards the channel wall. The shear layer reattached in the inter-obstacle spacing at $x/H = 2.5$ as observed from the pigment accumulation. This location is in good agreement with the LDA observations. The three vector plots show that the centres of the two recirculations are at about the same location. If the wake vortex was closed, the centres of the recirculations would shift towards the symmetry line for cross-sections at increasing height $y/H$. This shift is not observed, which means that the wake vortex is not closed at its top. The results indicate that the wake vortex consists of two separate spirally wound vortices with origins at the channel floor and that their endings are diffused in the downstream free shear layer.

The vector plots further show that the streamlines in the inter-obstacle space upstream of the cube are more or less parallel and undistorted for $y/H = 0.75$, with the exception of the wake vortex region and close to the windward face, whilst the streamlines are significantly curved in the plane $y/H = 0.25$. This curvature indicates that much of the fluid is advected away along the side whilst, at higher locations, much more fluid flows over the obstacle top.

The co-rotating horseshoe vortices can hardly be seen from the $u$-component at $y/H = 0.25$ since no local acceleration in the streamwise direction is generated by this vortex structure. This means that the vortex is advected away with the velocity of the bypassing flow.

### 3.2. Dynamic behaviour: vortex shedding

Flow instabilities which are initiated at the side faces caused the flow to fluctuate in a periodic manner. These coherent structures in the wake flow were detected from power density spectra of the time series of the spanwise velocity component. Since the highly turbulent flow separated from the sides of all cubes, vortex shedding occurred at a broader range of frequencies. The dominant characteristic frequency was derived from the location in the spectrum which corresponded to the maximum energy. Long time-averaged spectra were obtained from time durations of 500,000 data points which corresponded to about 20,000–40,000 vortex shedding cycles. This number of realizations was required to ensure a sufficiently large signal-to-noise ratio. A slotting, sample-and-hold and resampling method were compared to justify the accuracy of the calculated power density spectra, and thus the accuracy of the wake frequencies (Absil, 1996). The three methods reproduced the wake frequencies within 0.5 Hz. This value also pertains to the uncertainty of estimating the frequencies from the spectra and the total experimental uncertainty involved. A typical example of a power density spectrum is given in Fig. 9. The coherent structure in the flow (vortex shedding) is apparent from the increased activity around $f = 27$ Hz. The dashed line shows the filtered power density spectrum which corresponds to the contributions from the incoherent structures in the flow.

The wake frequencies were measured for a range of flow rates. These frequencies were made dimensionless with the bulk velocity and the cube size to yield the Strouhal number, $\mathrm{St} = Hf/u_B$. The Strouhal numbers are plotted versus the Reynolds number in Fig. 10. All results shown were determined from 500,000 data points. When an experimental uncertainty of 5% is taken into account, a constant Strouhal number of $\mathrm{St} = 0.109$ is found for the Reynolds number range of $2000 < \mathrm{Re}_H < 6000$. The deviations for $\mathrm{Re}_H < 2000$ are explained by larger experimental uncertainty or possible Reynolds number effects.

It is noted that the power density spectrum in Fig. 9 follows the $-5/3$ distribution in the inertial sub-range, which is usually found in non-shedding flows away from a solid wall at high Reynolds numbers. Fig. 9 also shows that the noise level becomes important around the truncation of the spectrum at $\Phi \approx 0.03$. A check on aliasing effects showed that the measurements were not seriously affected.

### 3.3. Second order moments

Grey-value representations of the Reynolds normal stresses $\overline{u'^2}$ and $\overline{w'^2}$ in the plane of symmetry, given in Fig. 11, directly show the anisotropy of the turbulent stress field. Note that both plots are presented at the same scale to allow a quantitative comparison. While the streamwise fluctuations $\overline{u'^2}$ become largest in the shear layer and horseshoe vortex region, the fluctuations in the spanwise velocity $\overline{w'^2}$ exhibit maxima where the side shear layers interfere, which is approximately around the reattachment point $x/H = 2.5$, and in front of the cube where the oncoming flow impinges on the front face. The vortex shedding from the lateral faces caused significant fluctuations in the $z$-direction. However, the fluctuations $\overline{w'^2}$ in the wake vortex region are rather small. Apparently, the unstable shedding behaviour is only prevalent in the shear layer enveloping the arc vortex and is almost diminished at the centreline

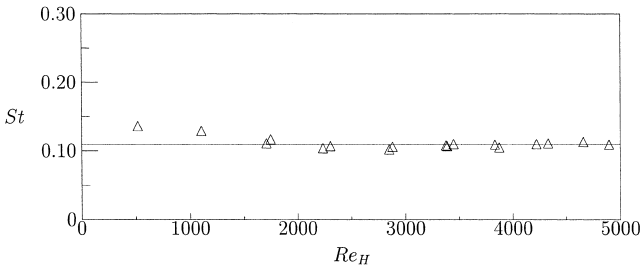


Fig. 10. Strouhal numbers ($\mathrm{St} = Hf/u_B$) versus the Reynolds number $\mathrm{Re}_H$. The solid line indicates the averaged value of $\mathrm{St} = 0.109$.

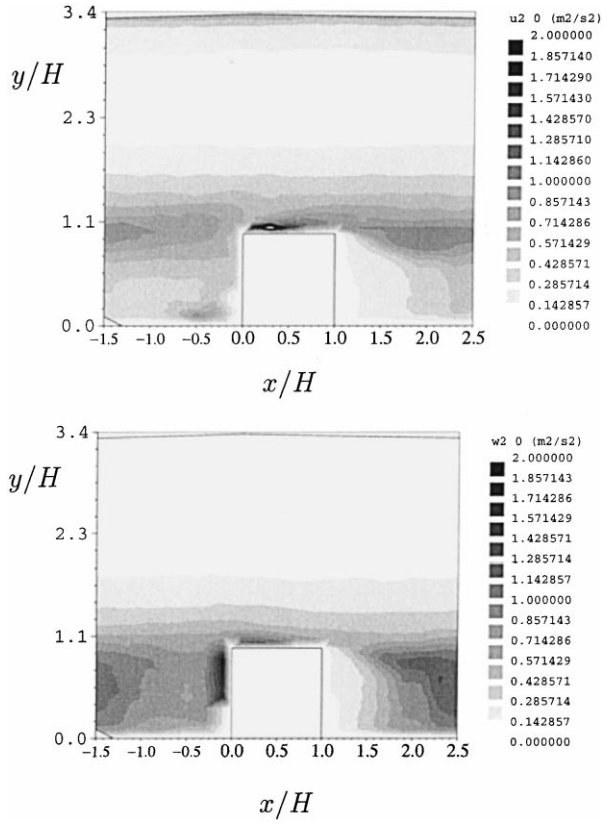


Fig. 11. Grey-values plots of the Reynolds normal stresses $\overline{u'^2}$ (upper plot) and $\overline{w'^2}$ (lower plot) for one spatial period at the symmetry plane $z/H = 0$.

$z/H = 0$. A qualitatively similar maximum in the spanwise velocity fluctuations around the reattachment point was also observed for a single wall-mounted cube in a fully developed turbulent channel flow (Martinuzzi, 1992). For this single-cube configuration, the mechanism of vortex shedding contributed also to the production of turbulence. The maxima in $\overline{u'^2}$ in the vicinity of the top face, where the shear layer separates and subsequently reattaches, are accompanied by a strong streamwise velocity gradient $\partial\overline{u}/\partial x$, see Fig. 4, leading to large values of the streamwise normal stress production term $\overline{u'^2}(\partial\overline{u}/\partial x)$. Although the velocity gradient diminishes further downstream in the shear layer, $\overline{u'^2}$ contributes still significantly to the streamwise normal stress production.

Measurement of the Reynolds normal stresses $\overline{v'^2}$ with the prism cube in the triangular region provided the third component for the turbulent kinetic energy, $k = 0.5\,(\overline{u'^2} + \overline{v'^2} + \overline{w'^2})$. It is noted that the values of $\overline{v'^2}$ obtained with the reconstruction technique were not accurate enough and are, therefore, not considered in this paper. Values of $k$ are given in Fig. 12 in the two triangles in front and in the wake of the obstacle. In the remaining part of the spatial period, the turbulent kinetic energy is approximated with $k_{2D} = 0.75\,(\overline{u'^2} + \overline{w'^2})$, where $\overline{u'^2}$ and $\overline{w'^2}$ were obtained from the LDA measurements with the probe in the standard orientation. These values of $k_{2D}$ are also given in Fig. 12. Although the above assumption is not fully accurate, particularly in the wake and reattachment region (see Fig. 11) the agreement between $k$ and $k_{2D}$ is sufficiently good (differences are at maximum 10%) to allow at least a qualitative interpretation of the turbulent kinetic energy field with $k_{2D}$.

The turbulent kinetic energy above the cubes (the core region of the channel) is rather small and increases gradually towards the opposing channel wall. The large Reynolds normal stresses found in the shear layer region and around the reattachment point lead to local maxima in the turbulent kinetic energy. A maximum in $k$ was found downstream in the shear layer at approximately one cube distance behind the leeward face where the shear layer is broadening and the turbulence level is decaying due to turbulent advection. The large values of $k$ in the horseshoe vortex region at the windward face of the obstacle indicate that this vortex structure is unstable and highly turbulent. Unstable behaviour of the horseshoe vortex was also observed for a single cube in a fully developed channel flow (Larousse et al., 1991; Martinuzzi, 1992). For this

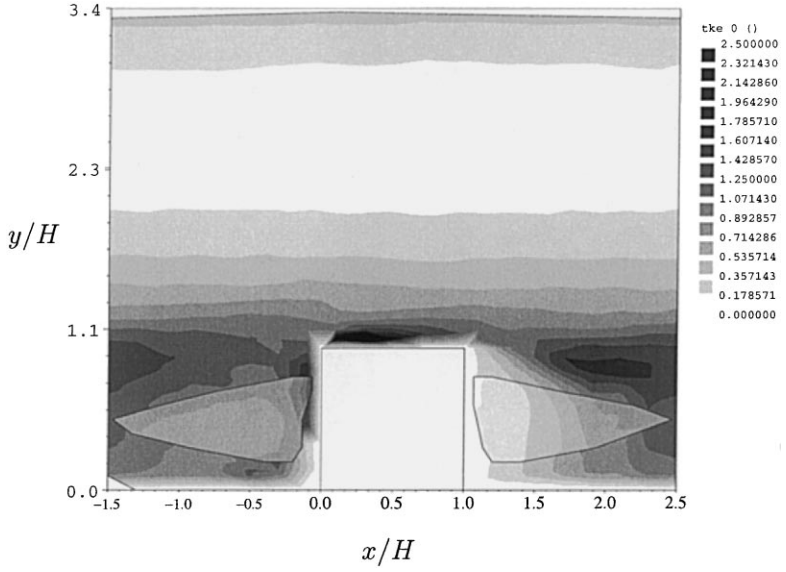


Fig. 12. Turbulent kinetic energy $k$ for one spatial period in the symmetry plane $z/H = 0$. The $k$-values in the triangular regions were determined from three velocity components, i.e. $k = 0.5(\overline{u'^2} + \overline{v'^2} + \overline{w'^2})$, the values in the remaining region were based on two velocity components, i.e. $k = 0.75(\overline{u'^2} + \overline{w'^2})$.

single cube, a bimodal non-periodic behaviour of the velocity components was observed which was attributed to the flipping between the two flow modes. In the case of a spatially periodic matrix flow, no bimodal behaviour was detected from the measured probability density functions in the horseshoe vortex region.

The turbulent kinetic energy, $k_{2D} = 0.75\,(\overline{u'^2} + \overline{w'^2})$ in the $xz$-plane is given in Fig. 13 for one half of a spatial period in the cube matrix for $y/H = 0.25$, 0.50 and 0.75. The flow impingement at the windward obstacle face caused local maxima in $k$, in particular at $y/H = 0.50$. The increased turbulent kinetic energy at $y/H = 0.25$ close to the front face of the cube is attributed to the horseshoe vortex. Similar to the top face, the local maxima close to the sides were caused by the intermittent reattachment of the shear layers which were separated at the sharp leading side edges. Flow instabilities at these faces are amplified and initiate the vortex shedding from the trailing side edges. The high turbulence levels directly behind these faces are, therefore, explained by the periodically fluctuating velocities. Again the turbulent kinetic energy is rather low in the centre of the wake vortex indicating that the perturbations induced by the vortex shedding are damped out. High $k$-concentrations were found at the symmetry-line at approximately $x/H = 2$ which is mainly due to the turbulent interaction between both side shear layers.

The Reynolds shear stress $\overline{u'w'}$ exhibits maxima at locations of large curvature of the mean streamlines. For example, at the obstacle windward face, the flow is directed around the cube causing large values in $\overline{u'w'}$, see Fig. 14 (the figures show isovalue plots of the Reynolds shear stress $\overline{u'w'}$ at $y/H = 0.25$, 0.5 and 0.75). The strong interaction between the wake vortex and the shear layer caused the maxima in the obstacle wake. The maxima shift towards the plane $y/H = 0$ where the flow reattaches and gradually move outwards to locations closer to the

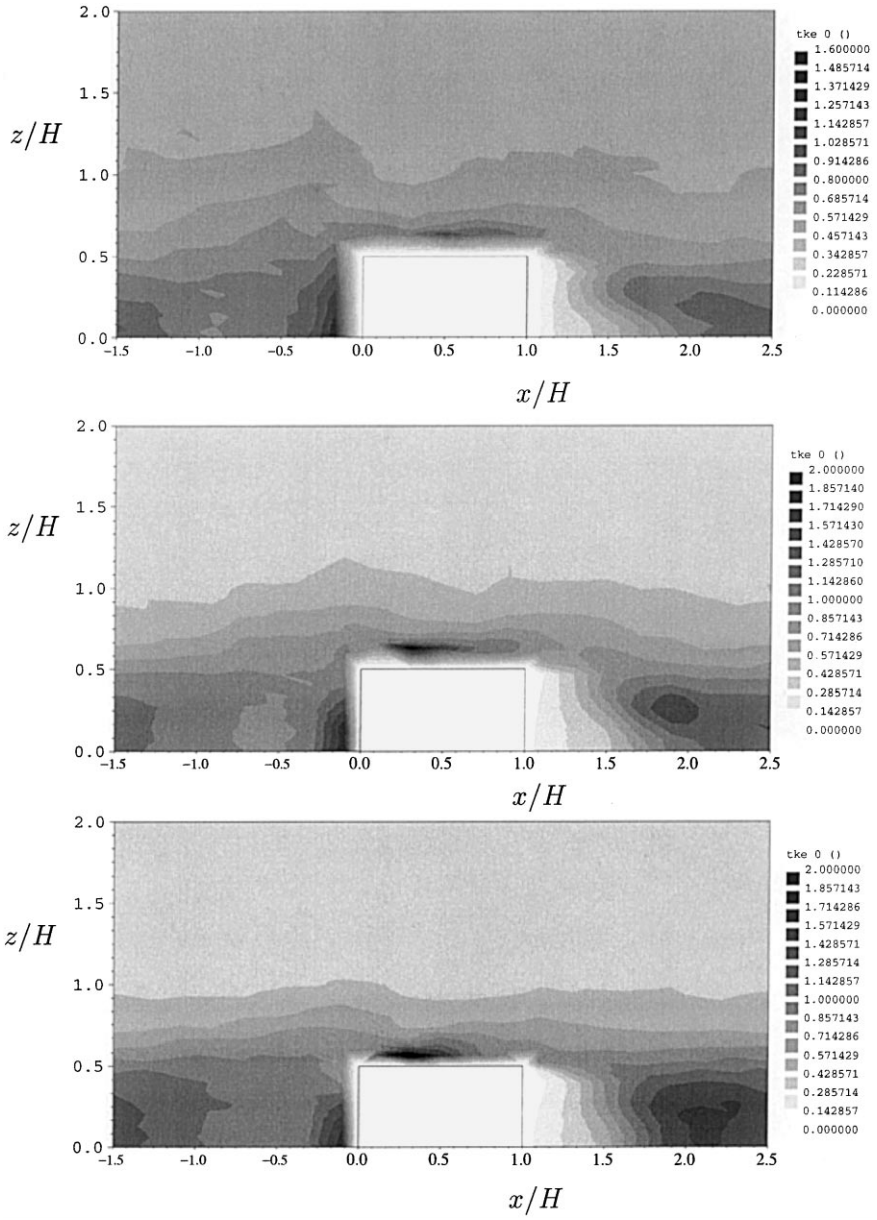


Fig. 13. Grey-values plot of the turbulent kinetic energy $k_{2D} = 0.75\,(\overline{u'^2} + \overline{w'^2})$ in the $xz$-plane for one half of a spatial period in the matrix for (a) $y/H = 0.25$, (b) $y/H = 0.50$ and (c) $y/H = 0.75$.

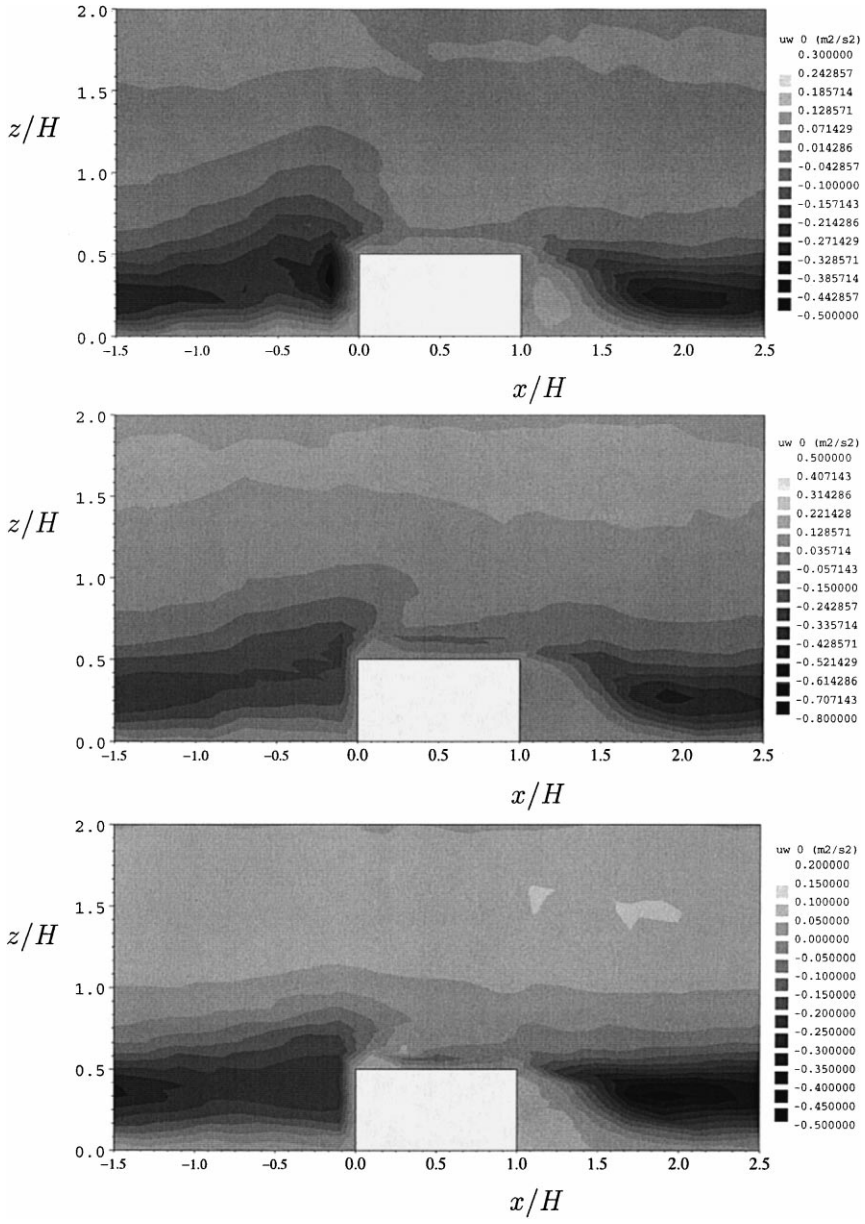


Fig. 14. Grey-value representation of the Reynolds shear stresses $\overline{u'w'}$ in the $xz$-plane for one half of a spatial period in the matrix for (a) $y/H = 0.25$, (b) $y/H = 0.50$ and (c) $y/H = 0.75$.

cube front. The distribution of the shear stress component $\overline{u'v'}$ is given in Fig. 15 for $x/H = 0.5$. These principle values were measured with the prism cube when the measuring volume was reflected into the second quadrant, the side area of the cube (see Fig. 2). The values were again obtained only in the triangular-shaped region due to the geometrical restrictions of the method. The shear stress reaches its maximum in the vicinity of the first horseshoe vortex.

### 3.4. Vorticity fields

The grey-values representations of the normal component of the vorticity vector $\overline{\omega}, \omega_y = (\partial w/\partial x) - (\partial u/\partial z)$, given in Fig. 16, show large vorticity concentrations in the near obstacle wake directly behind the side faces at locations where the velocity field exhibits strong spatial gradients. These maxima coincide with maxima in the turbulent quantities, represented by $k$. The vorticity concentrations at the side faces close to the

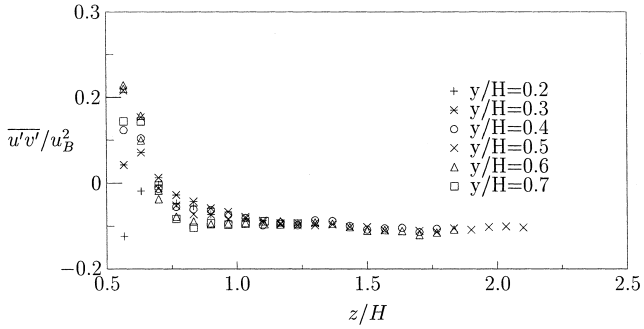


Fig. 15. Profiles of the Reynolds shear stresses $\overline{u'v'}$ at $x/H = 0.5$ (measured with the prism cube).

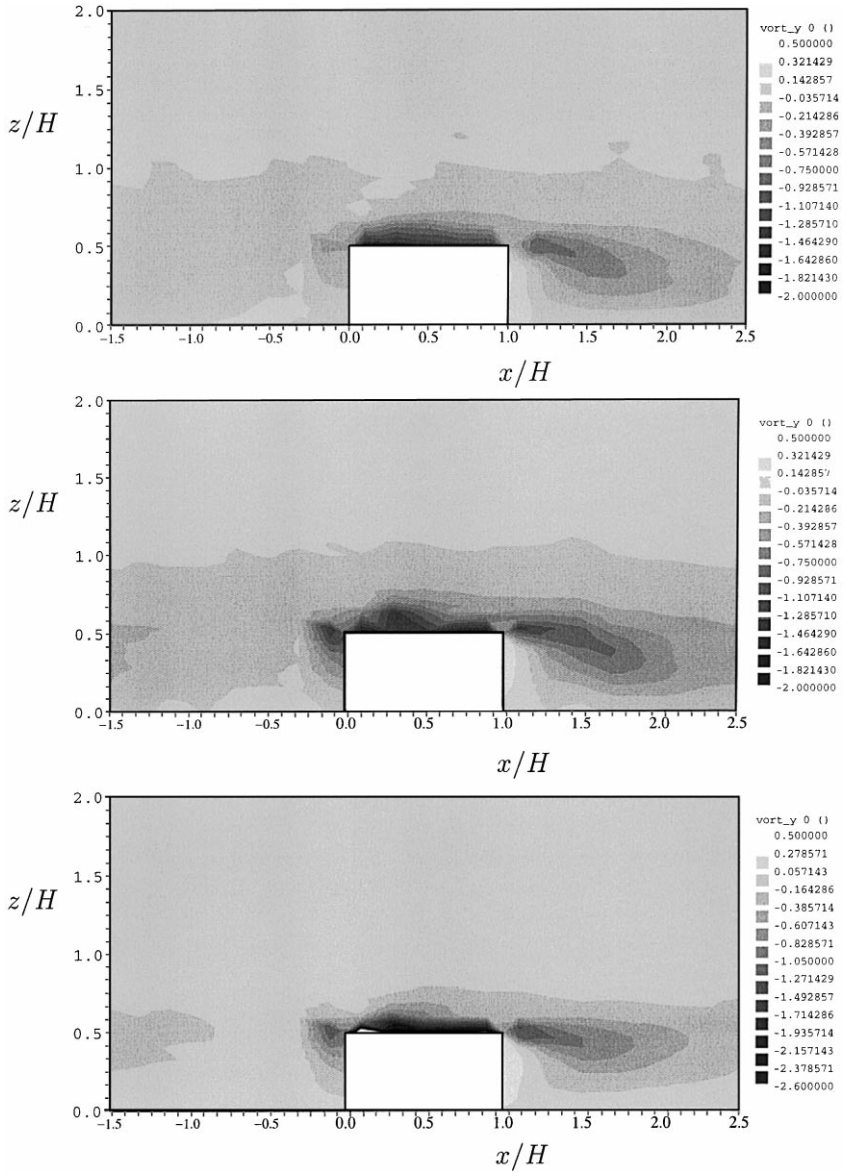


Fig. 16. Vorticity $\omega_y = ((\partial w/\partial x) - (\partial u/\partial z))$ in the $xz$-plane for one half of a spatial period in the matrix for (a) $y/H = 0.25$, (b) $y/H = 0.50$ and (c) $y/H = 0.75$.

leading edges are due to the rotating side vortices. A higher vorticity is also seen downstream at the back half of the side faces, though these values are somewhat contaminated by artifacts caused by the discontinuity in the velocity field: the velocity measurements were performed up to 1 mm from the side edges.

## 4. Convective heat transfer

The heat transfer was measured at one powered cube located in the spatially periodic matrix flow, while all the other cubes remained unpowered. The inlet temperature was used as a reference which, in this case, equals the adiabatic surface temperature (Moffat and Anderson, 1990). The heat transfer measurements were reproduced at different cubes in separate experiments and the results were well within the 10% uncertainty limit. Heat transfer experiments were performed in the Reynolds number range of $2380 < \mathrm{Re}_H < 5280$. The temperature of the copper core was kept at 75.0°C for all heat transfer measurements. The inlet temperature ranged between 19°C and 21°C, the measured actual value was used in the data processing. The surface temperature distributions were validated with liquid crystal measurements, as described in Meinders et al. (1997).

The surface-averaged heat transfer coefficient was derived from the surface integrated convective heat flux and surface temperature. The cube-averaged heat transfer coefficients were derived in a similar way, but the convective heat flux and surface temperature are then an average over all the five faces of the cube exposed to the air flow. The results, represented as the dimensionless Nusselt number ($\mathrm{Nu}_H = hH/\lambda$, where $h$ is the heat transfer coefficient, $H$ is the cube size and $\lambda$ is the thermal conductivity of air), are shown in Fig. 17 as a function of the Reynolds number $\mathrm{Re}_H$. Despite a small experimental uncertainty, the data follow a systematic and monotonic increase with Reynolds number. However, the range of Reynolds numbers considered is insufficient to establish a credible

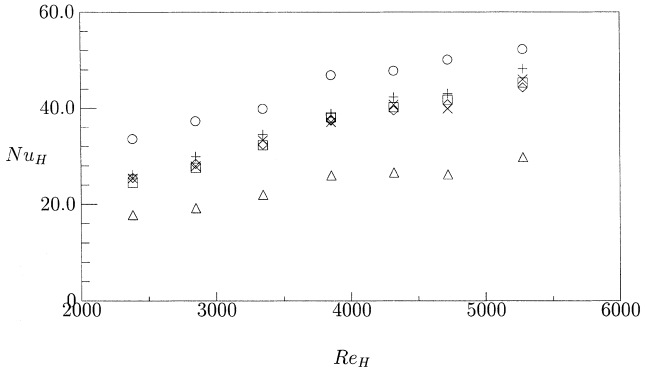


Fig. 17. Surface- and cube-averaged Nusselt number ($\mathrm{Nu}_H = \bar{h}H/\lambda$) as a function of the Reynolds number $\mathrm{Re}_H$: (+) side (north), (○) front, (×) side (south), (△) rear, (□) top and (◇) cube average.

correlation and we confined our attention to discussing the differences between the Nusselt numbers at different cube faces. A large Nusselt number found at the front face is indicative of the impinging flow at this face. The side and top faces typically have the lowest averaged Nusselt number which is due to the flow reversal, as shown later. The face-averaged heat transfer at the rear face is the lowest of all faces. The small deviations in the face-averaged Nusselt numbers can be traced back to deviations in the power supply. The sum of the total convective and radiative heat transfer from the five faces exposed to the air flow is denoted as (+) in Fig. 18 as a function of the Reynolds number $\mathrm{Re}_H$. The total supplied power to the heat source in the matrix cube, which is the product of the voltage drop and the current, is given in the same figure, indicated with (○). The difference between both the values is the heat leakage through the sixth face (which is the interface between the channel wall and the cube in question) and consists of conduction losses through the base plate and lead wires. For all considered Reynolds numbers, this heat loss is in the order of magnitude of 10–15%, where the smaller values pertain to the higher Reynolds numbers and vice versa.

Distributions of the heat transfer coefficient are shown along the paths ABCDA and ABCD in Fig. 19 for different Reynolds numbers. Path ABCDA denotes a cross-section parallel to the base plate at $y/H = 0.5$, path ABCD denotes a cross-section perpendicular to the base plate at the symmetry plane $z/H = 0$. The profiles are normalized with the cube-averaged heat transfer coefficient for the corresponding Reynolds number, as given in a dimensionless form in Fig. 17, and collapse within the experimental uncertainty. This suggests that the local heat transfer characteristics are similar throughout the range of Reynolds numbers considered ($2380 < \mathrm{Re}_H < 5280$). Because of this similarity, the discussion can be focussed on one characteristic distribution of the

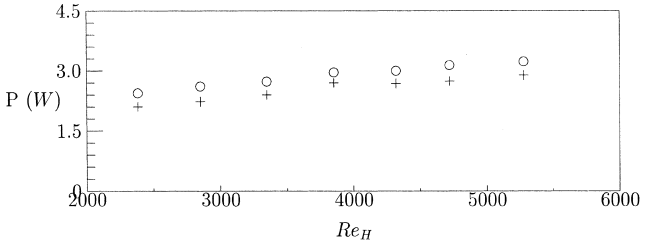


Fig. 18. Total supplied power (○) and the total heat through the five faces of the cube exposed to air flow (+) as a function of the Reynolds number $\mathrm{Re}_H$.

local heat transfer coefficient, related to the characteristic flow field. Fig. 19 reveals that the heat transfer coefficient distributions show large spatial gradients at a relatively small surface area, which reflects a complexity of the separating flow structure around the matrix cube. Despite this variation, the heat transfer displays a full symmetry with respect to the horizontal symmetry plane (at $z/H = 0$) indicating that local buoyancy effects are negligible. The flow is, therefore, classified as forced convection for all Reynolds numbers considered. This is also shown from the ratio of the Grashof number to the square of the Reynolds number, which can be used as a criterion for estimating the intensity of buoyant convection relative to forced convection. In the present case this ratio is much smaller than 1, i.e. $\mathrm{Gr}/\mathrm{Re}^2 = Hg\Delta T/TU^2 \approx 0.001$, where $g$ denotes gravity, $\Delta T$ the temperature difference between the flow and the object, $T$ the absolute temperature of the object, and $U$ the characteristic velocity of the flow).

As mentioned earlier, the heat transfer at the windward face (FRONT) benefits from the turbulent flow impingement and is the largest compared to the other faces. The peaks towards the side edges, see the upper figure in Fig. 19, are due to a local acceleration of the fluid, and thus cause a local increase in the heat transfer coefficient. Close to the mounting wall edge, the heat transfer coefficient shows a local minimum (the front face in the lower plot of Fig. 19) which is traced back to the presence of the horseshoe vortex. Heat convected away from the hot cube surface recirculates in the vortex causing the local fluid temperature to rise. This increased temperature level prevents a removal of heat at this location. A similar observation was made for the side faces (SIDES) of the cube. The side recirculations acted as insulation layers and, therefore, caused local minima close to the leading edge. In contrast, the fresh air from the intermittent reattaching shear layer at approximately 5 mm downstream towards the trailing edge caused the local maxima in the heat transfer coefficient. Similar features were found at the top face, shown in the lower plot in Fig. 19 (TOP). The bound vortex, located in the vicinity of the top leading edge, caused the heat transfer to become minimum at about the centre of the vortex core. The subsequent maximum is due to the reattachment of the separated shear layer. The convective heat transfer from the leeward face is the lowest compared to other faces, which are mainly attributed to the wake vortex. The recirculating heat also prevented a beneficial cooling at this face.

## 5. Conclusions

The flow field structure and distributions of the heat transfer coefficient of a wall-mounted cube in a spatially periodic matrix flow were studied experimentally. It is shown that the flow in the immediate proximity of the obstacle is characterized by a two-cell structure, which is created by the shear layer reattachment in the inter-obstacle space. A horseshoe-type vortex originates at the front face; an arc-shaped vortex exists in the wake. Flow separation at the sharp leading top and side edges causes flow recirculations close to the edges and subsequent reattachment at the faces more downstream. For the configuration considered, visible vortex shedding is detected in the wake of the cube. The typical Strouhal number of the shedding vortices is $\mathrm{St} = 0.109$. The periodic fluctuations caused by the vortex shedding and the high velocity gradients are believed to be the major cause of high turbulent kinetic energy in the free shear layers in the wake of the cube. The differences in the flow structure around the cube cause large gradients in the distributions of the local heat transfer coefficient. Similarity of these distributions, scaled with the cube-averaged heat transfer coefficient, shows no Reynolds number

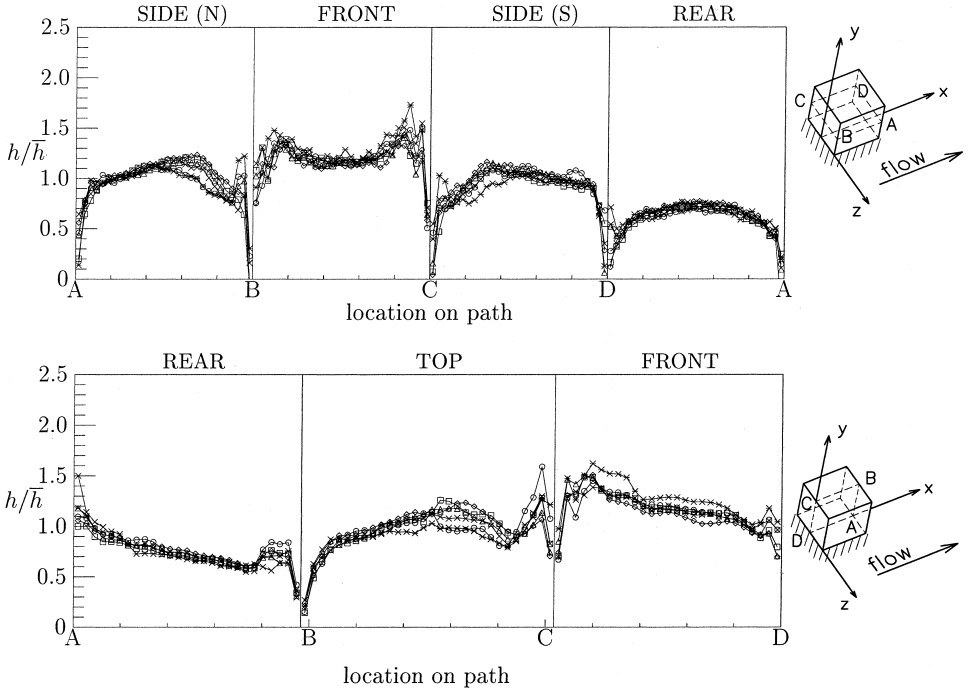


Fig. 19. Heat transfer coefficient distributions along paths ABCDA and ABCD as a function of the Reynolds number $Re_H$: (*) 2851, (○) 3348, (×) 3854, (△) 4321, (□) 4722 and (◇) 5279.

effects in the range investigated ($2380 < Re_H < 5280$). Regions of intense flow recirculations with subsequent flow separation are characterized by relatively low values of the local heat transfer coefficient. In contrast, high heat transfer coefficients are found in areas where the flow reattaches.

## Acknowledgements

This work was financially supported by Philips, Nederlandse Philips Bedrijven, The Netherlands. Bart Hoek and Jaap Beekman are gratefully acknowledged for their technical contributions to the work.

## References

Absil, L.H.J., 1996. Analysis of the laser Doppler measurement technique for application in turbulent flows. Ph.D. Thesis, Faculty of Aerospace, Delft University of Technology.

Anderson, A.M., Moffat, R.J., 1990. Convective heat transfer from arrays of modules with non-uniform heating: experiments and models. Ph.D. Thesis, Report No. HMT-43.

Anderson, A.M., Moffat, R.J., 1992. The adiabatic heat transfer coefficient and the superposition kernel function: part I-Data for arrays of flatpacks for different flow conditions. J. Electronic Packaging 114, 14–21.

Castro, I.P., Robins, A.G., 1977. The flow around a surface-mounted cube in uniform and turbulent streams. J. Fluid Mech. 79 (2), 307–335.

Durst, F., Melling, A., Whitelaw, J.H., 1976. Principles and Practise of Laser Doppler Anemometry. Academic Press, New York.

Garimella, S.V., Eibeck, P.A., 1990a. Heat transfer characteristics of an array of protruding elements in single phase forced convection. Int. J. Heat and Mass Transfer 33 (12), 2659–2669.

Garimella, S.V., Eibeck, P.A., 1990b. Effect of spanwise spacing on the heat transfer from an array of protruding elements in forced convection. Int. J. Heat and Mass Transfer 34 (9), 2427–2430.

Hussein, H.J., Martinuzzi, R.J., 1996. Energy balance for turbulent flow around a surface mounted cube placed in a channel. Phys. Fluids 8 (3), 764–780.

Larousse, A., Martinuzzi, R., Tropea, C., 1991. Flow around surface-mounted, three-dimensional obstacles. In: Eighth Symposium on Turbulent Shear Flows. TU-Munich/Germany, vol. 1, pp. 14-4-1/14-4-6.

Martinuzzi, R.J., 1992. Experimentelle Untersuchung der Umstroming wandgebundener, rechteckiger, prismatischer Hindernisse. Ph.D. Thesis, Erlangen, Germany.

Martinuzzi, R.J., Tropea, C., 1993. The flow around surface mounted, prismatic obstacles placed in a fully developed channel flow. J. Fluids Eng. 115, 85–92.

Meinders, E.R., van der Meer, T.H., Hanjalić, K., Lasance, C.J.M., 1997. Application of infrared thermography to the evaluation of local convective heat transfer on arrays of cubical protrusions. Int. J. Heat and Fluid Flow 18 (1), 152–159.

Meinders, E.R., van der Meer, T.H., Hanjalić, K., 1998a. Local convective heat transfer from an array of wall-mounted cubes. Int. J. Heat and Mass Transfer 41 (2), 335–346.

Meinders, E.R., Martinuzzi, R., Hanjalić, K., submitted. Experimental study of the local convective heat transfer from a wall-mounted cube in turbulent channel flow.

Meinders, E.R., 1998c. Experimental study of heat transfer in turbulent flows over wall-mounted cubes. Ph.D. Thesis, Faculty of Applied Sciences, Delft University of Technology, Delft, The Netherlands.

Moffat, R.J., Anderson, A.M., 1990. Applying heat transfer coefficient data to electronics cooling. J. Heat Transfer 112, 882–890.

Morris, G.K., Garimella, S.V., 1997. Composite correlations for convective heat transfer from arrays of three-dimensional obstacles. Int. J. Heat and Mass Transfer 40 (2), 493–498.

Okamoto, S., Tsunoda, K., Katsumata, T., Abe, N., Kijima, M., 1996. Turbulent near-wakes of periodic array of square blocks on a plate. Int. J. Heat and Fluid Flow 17, 211–218.